AIAA JOURNAL
Vol. 31, No. 8, August 1993

Nonlinear Large Amplitude Aeroelastic Behavior of Composite Rotor Blades

Taehyoun Kim* and John Dugundji†
Massachusetts Institute of Technology, Cambridge, Massachusetts 02139

An investigation is made of the nonlinear, large amplitude aeroelastic behavior of hingeless composite rotor blades during hover. The aeroelastic model is capable of dealing with large vibration amplitudes as well as large static deflections including transverse shear and warping deformation and is based on an Euler angle formulation of the basic large deflection equations together with a harmonic balance, finite difference, and Newton-Raphson technique. Nonlinear stall aerodynamics is included by use of the ONERA airforces model. Analysis of large amplitude limit cycles that evolve from linear flutter solutions is performed on a $[0/90]_{3S}$ graphite/epoxy composite blade model. Numerical results indicate that the nonlinear stall is dominant at moderate amplitudes, but that nonlinear static-dynamic couplings in the structure, which bring a softening effect into the general aeroelastic behavior, could be equally important at large amplitudes.

Nomenclature

b	= semichord
c	= chord
E_{ij}	= beam stiffness matrix elements
$\underline{e}$	= hinge offset
e_a	= distance between the reference line and the aerodynamic center
F_1, F_2, F_3	= force resultant components in local axes
F_{NC}, F_C	= noncirculatory and circulatory air loads
g	= gravity
k	= reduced frequency, $\omega b/V_0$
l	= beam length
M_1, M_2, M_3	= moment resultant components in local axes
m_i^L	= applied moments in local axes
$\boldsymbol{m}^G$	= applied moment vector in global axes
N_B	= number of blades
p_i^L	= applied loads in local axes
$\boldsymbol{p}^G$	= applied load vector in global axes
s	= arc length
$[T]$	= transformation matrix
T_{ij}	= transformation matrix elements
u, v, w	= displacements along x, y, z axes
V	= resultant air velocity at aerodynamic center
V_0	= static part of V
V_2, V_3	= tangential and normal components of V
v_i	= inflow velocity
X	= vector of unknowns
x, y, z	= global coordinates
α	= angle of attack at the aerodynamic center
β_p	= blade preconing angle
ΔC_D	= deviation of actual static drag curve from linear static drag
ΔC_z	= deviation of actual static lift or moment curve from linear static lift or moment
Γ_{1z}	= linear circulatory lift or moment circulation
Γ_{2z}	= stalled circulatory lift or moment circulation
Γ_{D1}	= linear drag circulation
Γ_{D2}	= nonlinear drag circulation
$\gamma_{\xi\eta}, \gamma_{\xi\zeta}$	= beam shear strains
ϵ	= beam extension strain
$\dot{\epsilon}_e$	= blade equivalent pitch rate
κ_ξ	= twist rate around ξ axis
$\kappa_\eta, \kappa_\zeta$	= bending curvatures around η, ζ axes
ξ, η, ζ	= local coordinates
ρ	= blade or air density
τ	= nondimensional time, $V_0 t/b$
ψ, β, θ	= Euler angles
Ω	= blade rotational speed
ω	= frequency
ω_ξ	= blade rotation around ξ axis
$(\dot{})$	= derivative with respect to real time

Subscripts

$0, s, c$	= mean, sine, and cosine components, respectively

I. Introduction

MOST analysis of helicopter blade aeroelastic behavior is traditionally based on small amplitude approximations about a given static deformation of the blade using moderate deflection formulations and linear aerodynamic theories. However, under certain circumstances such as high angle-of-attack thrust, maneuvering, or gust, a nonlinear large amplitude limit cycle may occur at different flight conditions than linear prediction would predict. In the literature, there has been only limited interest in exploring this nonlinear aeroelastic behavior and its transition from linear behavior. A simple such analysis, dealing only with geometrical nonlinearities of the rigid blade, was given by Chopra and Dugundji.[1] Most recently, Dunn and Dugundji[2] have given a similar analysis for a fixed wing; this time dealing with aerodynamic stall effects only by use of the ONERA stall model introduced by Tran and Petot.[3] Also, Tang and Dowell[4] have introduced both structural nonlinearities and dynamic stall in their investigation of stall limit cycles and chaotic motion of flexible, nonrotating blades. The structural nonlinearities here were approximated by the moderate deflection equations developed by Hodges and Dowell,[5] and the dynamic stall was represented by the ONERA model. Both investigations on these nonrotating lifting surfaces had found that the effect of the dynamic stall in the overall aeroelastic limit cycle behavior is largely stiffening in moderate range of amplitudes, i.e., more dynamic pressure would be required to produce higher amplitudes once the onset of flutter has occurred. To better understand the impact of both nonlinear structure and aerodynamics, a nonlinear

Presented as Paper 92-2257 at the AIAA/ASME/ASCE/AHS/ASC 33rd Structures, Structural Dynamics, and Materials Conference, Dallas, TX, April 13-15, 1992; received Aug. 27, 1992; revision received Dec. 3, 1992; accepted for publication Dec. 3, 1992.

*Graduate Student, Department of Aeronautics and Astronautics. Member AIAA.

†Professor, Department of Aeronautics and Astronautics. Member AIAA.

aeroelastic analysis of rotating flexible blades representing full structural nonlinearities as well as dynamic stall would seem valuable at this point.

On the structural side, it has been known that under large static deflections, the natural frequencies and mode shapes of cantilever helicopter blades, particularly the fore-and-aft (lead-lag) and the torsional modes, show interesting characteristics that are not apparent from their vibration behavior as undeflected cantilever blades. See, for example, Loewy et al.,[6] Mathew and Loewy,[7] and Minguet and Dugundji.[8] Additionally, for large vibration amplitudes of these modes, their frequency, mean position, and mode shapes may change further. These effects of large vibration amplitudes were examined in a recent paper by Kim and Dugundji.[9] One of the findings was that in the presence of a moderate amount of static deflection, the first fore-and-aft mode of hingeless blades, which is an aeroelastically critical mode, may exhibit a softening phenomenon at large vibration amplitude levels.

The present paper incorporates the structural effects into a nonlinear, large amplitude flutter limit cycle analysis of rotating hingeless composite blades in the simple case of hover and is drawn from a more general aeroelastic investigation reported by Kim.[10] The aerodynamic nonlinearities involving stalling are included here using the ONERA stall model and assuming coefficients for NACA 0012 airfoil at low Reynolds numbers. The resulting analysis is solved by integration of the basic nonlinear equations, a harmonic balance method, and Newton-Raphson iterative technique. Numerical results are given for a two-bladed model of $[0/90]_{3S}$ graphite/epoxy layup that had also been used in Refs. 8 and 9. The objectives of the present paper are to develop a methodology for solving the nonlinear large amplitude aeroelastic problems of rotor blades and to identify and demonstrate new nonlinear aeroelastic phenomena of rotor blades.

II. Structural Modeling

To represent the nonlinearities due to large deflections and rotations as fully as possible, a set of 12 nonlinear differential equations developed by Minguet and Dugundji[8] is used in the present analysis. The governing equations are obtained by considering equilibrium, strain-displacement compatibilities, linear stress-strain relations of a blade element, and are not based on any ordering schemes that typify most of moderate deflection equations. All of the equations are derived based on the following transformation matrix that transforms the global coordinate x, y, z into the local one ξ, η, ζ, i.e.,

$$\begin{Bmatrix} i_\xi \\ i_\eta \\ i_\zeta \end{Bmatrix} = [T] \begin{Bmatrix} i_x \\ i_y \\ i_z \end{Bmatrix}$$

$$[T] = \begin{bmatrix} \cos\beta\cos\psi & \cos\beta\sin\psi & \sin\beta \\ -\cos\theta\sin\psi & \cos\theta\cos\psi & \sin\theta\cos\beta \\ -\sin\theta\sin\beta\cos\psi & -\sin\theta\sin\beta\sin\psi & \\ \sin\theta\sin\psi & -\sin\theta\cos\psi & \cos\theta\cos\beta \\ -\cos\theta\sin\beta\cos\psi & -\cos\theta\sin\beta\sin\psi & \end{bmatrix} \tag{1}$$

Here ψ, β, θ are the local Euler angles. When the preconing angle β_p is introduced for the blade, one has to define an additional transformation between the actual global coordinates x_0, y_0, z_0, and the global coordinates on the blade x, y, z (see Fig. 1) as

$$\begin{Bmatrix} i_\xi \\ i_\eta \\ i_\zeta \end{Bmatrix} = [T'] \begin{Bmatrix} i_{x0} \\ i_{y0} \\ i_{z0} \end{Bmatrix}$$

$$[T'] = \begin{bmatrix} T_{11} - \beta_p T_{13} & T_{12} & T_{13} + \beta_p T_{11} \\ T_{21} - \beta_p T_{23} & T_{22} & T_{23} + \beta_p T_{21} \\ T_{31} - \beta_p T_{33} & T_{32} & T_{33} + \beta_p T_{31} \end{bmatrix} \tag{2}$$

where it was assumed that $\cos\beta_p \approx 1$, and $\sin\beta_p \approx \beta_p$.

It has been noted that the structural model used in Refs. 8 and 9 does not include cross-sectional transverse shear and warping deformation.[11] These effects could be included to some extent, if desired, as follows. For the shear deformation, one can introduce the shear strains $\gamma_{\xi\eta}$, $\gamma_{\xi\zeta}$, and the axial strain ϵ in calculating the displacements x, y, z as

$$\begin{aligned} \frac{\partial x}{\partial s} &= (1+\epsilon)(T_{11} + T_{21}\gamma_{\xi\eta} + T_{31}\gamma_{\xi\zeta}) \\ \frac{\partial y}{\partial s} &= (1+\epsilon)(T_{12} + T_{22}\gamma_{\xi\eta} + T_{32}\gamma_{\xi\zeta}) \\ \frac{\partial z}{\partial s} &= (1+\epsilon)(T_{13} + T_{23}\gamma_{\xi\eta} + T_{33}\gamma_{\xi\zeta}) \end{aligned} \tag{3}$$

For the out-of-plane warping, a classical linear twist equation[12] is invoked to include a warping correction in the form of second derivative of the twist rate κ_ξ. To implement this correction within the current model, one should introduce two additional first-order differential equations and a term proportional to the second derivative within the equilibrium equation for the twisting moment M_1 as follows:

$$\frac{\partial \kappa_\xi}{\partial s} = \kappa_\xi', \qquad \frac{\partial \kappa_\xi'}{\partial s} = \kappa_\xi'' \tag{4}$$

$$M_1 = E_{44}\kappa_\xi + A\kappa_\xi'' + \text{coupling terms} \tag{5}$$

with additional boundary conditions,

$$\kappa_\xi(0) = 0, \qquad \kappa_\xi'(l) = 0$$

where A represents the warping coefficient (e.g., $-E_{55}c^2/12$, for a composite strip). When considered altogether, one can write the linear stress-strain relations for a composite blade as

$$\begin{bmatrix} F_1 \\ F_2 \\ F_3 \\ M_1 \\ M_2 \\ M_3 \end{bmatrix} - \begin{bmatrix} E_{14} \\ E_{24} \\ E_{34} \\ E_{44} \\ E_{45} \\ E_{46} \end{bmatrix} \kappa_\xi = \begin{bmatrix} E_{11} & E_{12} & E_{13} & 0 & E_{15} & E_{16} \\ E_{12} & E_{22} & E_{23} & 0 & E_{25} & E_{26} \\ E_{13} & E_{23} & E_{33} & 0 & E_{35} & E_{36} \\ E_{14} & E_{24} & E_{34} & A & E_{45} & E_{46} \\ E_{15} & E_{25} & E_{35} & 0 & E_{55} & E_{56} \\ E_{16} & E_{26} & E_{36} & 0 & E_{56} & E_{66} \end{bmatrix} \begin{bmatrix} \epsilon \\ \gamma_{\xi\eta} \\ \gamma_{\xi\zeta} \\ \kappa_\xi'' \\ \kappa_\eta \\ \kappa_\zeta \end{bmatrix} \tag{6}$$

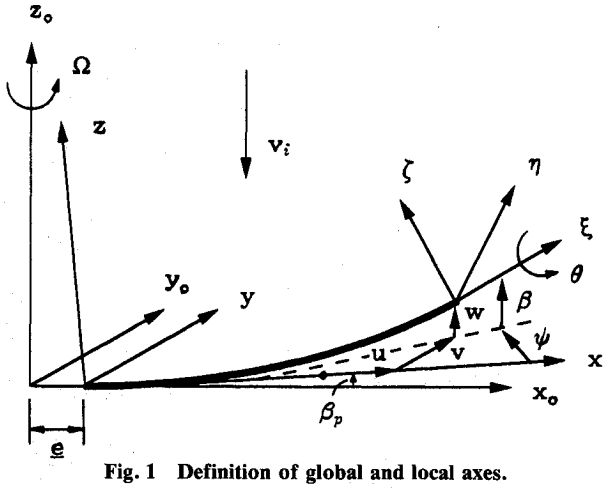

Fig. 1 Definition of global and local axes.

At any station, Eq. (6) can be inverted to give appropriate values of $[\epsilon\ \gamma_{\xi\eta}\ \gamma_{\xi\zeta}\ \kappa_\xi''\ \kappa_\eta\ \kappa_\zeta]^T$ for integrating the differential equations.

III. Inertial Modeling

Inertial load terms p_i^G and m_i^G can be obtained by evaluating acceleration of a particle on the blade in the rotating axis system and expressing the resulting forces and moments in it (see Fig. 1). That is,

$$p^G = -\int\int_A \rho a\, dA$$
$$m^G = -\int\int_A \rho p \times a\, dA \tag{7}$$

where

$$a = \frac{d^2 r}{dt^2} = \ddot{r} + 2\Omega \times \dot{r} + \Omega \times (\Omega \times r) + g i_{z0} \tag{8}$$

The vector r, which measures the distance from the origin to the particle of interest, can be represented in the global system x, y, z as

$$r(\eta, \zeta) = \begin{Bmatrix} x + \underline{e} \\ y \\ z - \beta_p \underline{e} \end{Bmatrix} + p(\eta, \zeta) \tag{9}$$

The vector p represents the radius of the particle from the reference axis on its cross section.

$$p(\eta, \zeta) = [T]^T \begin{Bmatrix} 0 \\ \eta \\ \zeta \end{Bmatrix} \tag{10}$$

The resulting inertial loads can be expressed either in local coordinates ξ, η, ζ or global coordinates x, y, z; the former being unwieldy and cumbersome to deal with in their original form. It can be shown that by utilizing orthogonality properties of the transformation matrix $[T]$ and its relation to the rotation matrix $[\omega]$, the local expressions can be simplified to a great extent.[10] The final local equations in this reduced form are more compatible with the 12 governing differential equations and reveal more clearly the individual terms from the linear and angular accelerations and centrifugal and Coriolis accelerations that are not very obvious in the global expressions.

IV. Aerodynamic Modeling

A. Dynamic Stall

For the present research, one needs an aerodynamic tool that can adequately describe both linear unstalled and nonlinear stalled aerodynamic loads with ease and simplicity. In particular, its form must be such that it can be immediately applied to the stability and response analysis for the composite rotor blades using a simple harmonic method. Recently, the ONERA Model that consists of two ordinary differential equations has found popularity.[2,4,13,14] One of the major advantages of the model is that by using the basic properties of the second-order differential equations it can adequately, if not precisely, generate stalled hysteresis loops without going into details of the unsteady aerodynamic theories. However, it is mentioned that most of the applications of the ONERA model in rotary wing problems have been exclusively focused on the periodic responses and their stabilities of forward flight cases. In forward flight, the dynamic stall phenomenon near the retreating blade side does not produce stall flutter because of its short period of presence. On the other hand, dynamic stall in hovering flight, if it ever exists, can develop into flutter oscillations. The periodic responses in this case are self-excited oscillations that are sustained over a long period of time. For a simple analysis of nonlinear flutter problems only the first few harmonics are adequate to capture the amplitude levels as well as the associated frequency and dynamic pressure. In the present analysis, only the first harmonics are extracted from the nonlinear ONERA model.

A nonlinear lift and moment model based on the ONERA equations and the harmonic balance method has been used by Dunn and Dugundji[2] for fixed-wing cases. The present one is a further extension of their model including the effects of large angle of attack, pulsating incoming velocity, stall delay, and drag stall as well. Following suggestions of Peters,[15] Petot and Dat,[16] and Barwey et al.,[17] the basic ONERA equations appropriate for rotary wing problems can be written as follows.

Lift and moment:

$$F_{NC} = \tfrac{1}{2}\rho S_z (s_z b \dot{V}_3 + l_z b V \dot{\epsilon}_e + k_z b^2 \ddot{\epsilon}_e)$$
$$F_C = \tfrac{1}{2}\rho S_z (V\Gamma_{1z} + V\Gamma_{2z}) \tag{11}$$

where

$$\Gamma_{1z} = a_{0z} V_0 \alpha_0 + \Gamma_{11z}$$
$$\dot{\Gamma}_{11z} + \lambda_z (V_0/b)\Gamma_{11z} = \lambda_z a_{0z} (V_0/b) V_3 + \lambda_z \sigma_z V_0 \dot{\epsilon}_e + \gamma_z a_{0z} \dot{V}_3 + \gamma_z \sigma_z b \ddot{\epsilon}_e$$
$$\ddot{\Gamma}_{2z} + a_z (V_0/b)\dot{\Gamma}_{2z} + r_z (V_0^2/b^2)\Gamma_{2z} = -r_z [(V_0^2/b^2)(V\,\Delta C_z) + e_z (V_0/b)(V \Delta \dot{C}_z)] \tag{12}$$

and the subscript $z = L$ or M for lift or moment.

Drag:

$$D = \tfrac{1}{2}\rho c (V\Gamma_{D1} + V\Gamma_{D2}) \tag{13}$$

where

$$\Gamma_{D1} = V C_{D0}$$
$$\ddot{\Gamma}_{D2} + a_D (V_0/b)\dot{\Gamma}_{D2} + r_D (V_0^2/b^2)\Gamma_{D2} = -[r_D (V_0^2/b^2)(V\,\Delta C_D) + e_D (V_0/b)\dot{V}_3] \tag{14}$$

Here, using Dunn and Dugundji[2] and Barwey et al.[17] the following coefficients have been assumed for NACA 0012 airfoil at low Reynolds numbers ($Re \leq 3.4 \times 10^6$):

$$S_L = c, \qquad s_L = \pi, \qquad l_L = 0, \qquad k_L = 0.5\pi$$

$$a_{0L} = \sigma_L = 5.9$$

$$\lambda_L = 0.15, \qquad \gamma_L = 0.55$$

$$a_L = 0.25 + 0.4(\Delta C_L)^2$$

$$r_L = [0.2 + 0.23(\Delta C_L)^2]^2$$

$$e_L = -2.7(\Delta C_L)^2$$

$$S_M = c^2, \qquad s_M = l_M = -(\pi/4), \qquad k_M = -(3\pi/16)$$

$$a_{0M} = \sigma_M = \lambda_M = \gamma_M = 0$$

$$a_M = a_L, \qquad r_M = r_L, \qquad e_M = e_L$$

$$C_{D0} = 0.014$$

$$a_D = 0.32$$

$$r_D = (0.2 + 0.1\Delta C_L^2)^2$$

$$e_D = -0.015\Delta C_L^2$$

ΔC_L, ΔC_M, and ΔC_D each represents the deviation of the linear static curve from the quasistatic curve for the lift, moment, and drag, respectively. It is noted that when no stall exists (i.e., $\Gamma_{2L} = \Gamma_{2M} = 0$) and the angle of attack is small, the preceding equations for the lift and moment reduce to the exact form of the Greenberg's expression with the first-order Padé approximation for the Theodorsen function $C(k)$. The normal downwash air velocity V_3 at the aerodynamic center appears as a boundary condition in the linear part of the lift equations, as does the so-called equivalent pitch rate $\dot{\epsilon}_e$.

B. Calculation of Air Velocities

The tangential and normal components of the air velocity at the aerodynamic center are represented as

$$V_2 = \Omega[(x + \underline{e} - z\beta_p)T_{22} + y(\beta_p T_{23} - T_{21})] + \dot{x}T_{21} + \dot{y}T_{22} + \dot{z}T_{23} + v_i(T_{23} + \beta_p T_{21})$$

$$V_3 = -\Omega[(x + \underline{e} - z\beta_p)T_{32} + y(\beta_p T_{33} - T_{31})] - \dot{x}T_{31} - \dot{y}T_{32} - \dot{z}T_{33} - \eta_r\dot{\epsilon}_e - v_i(T_{33} + \beta_p T_{31}) \tag{15}$$

and

$$V = \sqrt{V_2^2 + V_3^2} \tag{16}$$

Here the equivalent pitch rate $\dot{\epsilon}_e$ is given as

$$\dot{\epsilon}_e = \omega_\xi + \Omega(T_{13} + \beta_p T_{11}) \tag{17}$$

The inflow velocity v_i, which is assumed constant, can be obtained by considering a momentum balance along the circular ring element ds as follows.

$$4\pi\rho(x + \underline{e} - \beta_p z)v_i^2 = N_B[(\beta_p T_{21} + T_{23})p_2^L + (\beta_p T_{31} + T_{33})p_3^L] \tag{18}$$

The right-hand side, whether stall exists or not, is generally a complicated function of v_i itself, and does not render the equation to be solved explicitly for v_i. Hence, to get the exact solution, an iteration technique with appropriate initial guess should be used. Depending on the initial value guessed, the method usually converges within a few iterations. For example, the initial value of v_i can be assigned by solving the quadratic equation

$$8\pi(x + \underline{e} - \beta_p z)v_i^2 + N_B\Omega(x + \underline{e} - \beta_p z)^2 cC_{L\alpha}(T_{33} + \beta_p T_{31}) \times (v_i/V_2) - N_B\Omega^2(x + \underline{e} - \beta_p z)^2 cC_{L\alpha}(V_3/V_2) = 0 \tag{19}$$

in the linear unstalled region, or

$$8\pi(x + \underline{e} - \beta_p z)v_i^2 + N_B\Omega(x + \underline{e} - \beta_p z)^2 ca_{ss}(T_{33} + \beta_p T_{31}) \times (v_i/V_2) - N_B\Omega^2(x + \underline{e} - \beta_p z)^2 c[a_{ss}(V_3/V_2) + b_{ss}] = 0 \tag{20}$$

in the nonlinear stalled region. Again, these equations are obtained by considering the momentum balance of a ring element with small angle-of-attack approximation. In the first equation, the static lift curve is simply $C_{L\alpha}\alpha$, whereas in the second equation, it was assumed by a simple one-breakpoint approximation, $a_{ss}\alpha + b_{ss}$.

C. Local Aerodynamic Loads

When the local airloads in the local coordinates ξ, η, ζ are calculated the following assumptions are made. First, the apparent mass lift L_{NC} acts normal to the airfoil. Second, the circulatory lift L_C is normal to the resultant air velocity V, whereas the drag D is parallel to the resultant air velocity, see Fig. 2. The resulting local airloads are then expressed as

$$\begin{aligned} p_2^L &= L_C\sin\alpha - D\cos\alpha \\ &= \rho b[V_3(\Gamma_{1L} + \Gamma_{2L}) - V_2(\Gamma_{1D} + \Gamma_{2D})] \\ p_3^L &= L_C\cos\alpha + D\sin\alpha + L_{NC} \\ &= \rho b[V_2(\Gamma_{1L} + \Gamma_{2L}) + V_3(\Gamma_{1D} + \Gamma_{2D})] + L_{NC} \\ m_1^L &= M_C + M_{NC} + (p_3^L - L_{NC})e_a \\ &= 2\rho b^2 V(\Gamma_{1M} + \Gamma_{2M}) + M_{NC} + (p_3^L - L_{NC})e_a \end{aligned} \tag{21}$$

V. Harmonic Balance Method

A. Structural Part

All quantities are cast into their first harmonic forms

$$X(\Omega, \omega, t) = X_0(\Omega, \omega) + X_s(\Omega, \omega)\sin\omega t + X_c(\Omega, \omega)\cos\omega t \tag{22}$$

The dependency of X_0, X_s, X_c on frequency ω reflects the fact that the vibration components X_s and X_c could be large beyond the linearized small amplitude approximation and there could be nonlinear coupling between the static and vibration parts. The harmonic balance consists of substituting the preceding expression for 12 variables into the 12 (14 if warping and shear is included) governing equations and then retaining only the lowest harmonic terms. As was shown in Kim and Dugundji,[9] one needs an ordering scheme in discarding higher order, higher harmonic terms due to the presence of many

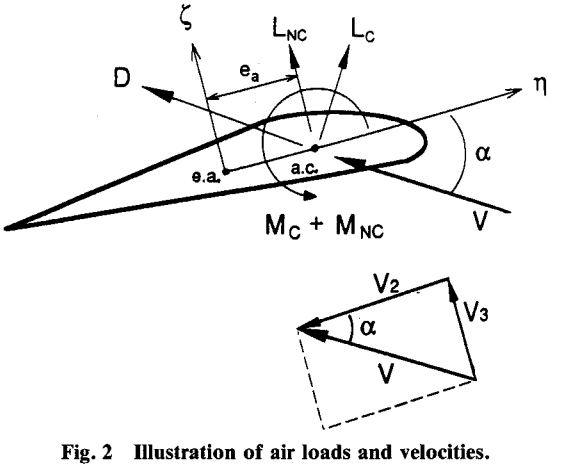

Fig. 2 Illustration of air loads and velocities.

multiplications involving two or even three harmonic functions associated with the transformation matrix elements. A third-order ordering scheme similar to the one in Ref. 9 is employed here, with the addition of cos ωt terms to account for phase shifts. It is emphasized that the ordering scheme still preserves the complete nonlinearities in large rotations and large displacements in the static sense, but only terms up to third order are kept in the dynamic counterparts. For example, according to this ordering scheme one does not have

$$\cos\theta \sim 1 - (\theta^2/2) + \text{HOT}$$

but rather

$$\cos\theta \sim \cos\theta_0 - \sin\theta_0\Delta\theta - \tfrac{1}{2}\cos\theta_0(\Delta\theta)^2 + (1/6)\sin\theta_0(\Delta\theta)^3 + \text{HOT}$$

where $\theta = \theta_0 + \Delta\theta$, the θ_0 and $\Delta\theta = \theta_s \sin\omega t + \theta_c \cos\omega t$ represent the static and dynamic components of θ, and HOT represents higher order terms.

B. Aerodynamic Part

For the harmonic balance of aerodynamic part, all quantities are expressed as

$$X(\Omega, k, \tau) = X_0(\Omega, k) + X_s(\Omega, k)\sin k\tau + X_c(\Omega, k)\cos k\tau \tag{23}$$

where k is the reduced frequency $= \omega b/V_0$, and τ is the nondimensional time $= V_0 t/b$. The effective angle of attack α is given by

$$\alpha = \tan^{-1}(V_3/V_2) \tag{24}$$

and is expanded in the first harmonic form

$$\begin{aligned}\alpha(\tau) &= \alpha_0 + \alpha_s \sin k\tau + \alpha_c \cos k\tau \\ &= \alpha_0 + \alpha_V \sin\varphi\end{aligned} \tag{25}$$

where

$$\begin{aligned}\alpha_V &= \sqrt{\alpha_s^2 + \alpha_c^2} \\ \varphi &= k\tau + \xi, \qquad \xi = \sin^{-1}(\alpha_c/\alpha_V)\end{aligned} \tag{26}$$

Next, assume harmonic motion for ΔC_z

$$\Delta C_z(\varphi) = \Delta C_{z0} + \Delta C_{zV_s}\sin\varphi + \Delta C_{zV_c}\cos\varphi \tag{27}$$

where by use of Fourier analysis,

$$\begin{aligned}\Delta C_{z0} &= \frac{1}{\pi}\int_{-\frac{\pi}{2}}^{\frac{\pi}{2}} \Delta C_z(\varphi)\, d\varphi \\ \Delta C_{zV_s} &= \frac{2}{\pi}\int_{-\frac{\pi}{2}}^{\frac{\pi}{2}} \Delta C_z(\varphi)\sin\varphi\, d\varphi \\ \Delta C_{zV_c} &= \frac{2}{\pi}\int_{-\frac{\pi}{2}}^{\frac{\pi}{2}} \Delta C_z(\varphi)\cos\varphi\, d\varphi\end{aligned} \tag{28}$$

In general, ΔC_z can be described in any manner desired. For simplicity, following Dunn and Dugundji,[2] ΔC_z was described by simple two straight line fits of low Reynolds number static curves of a NACA 0012 airfoil (see Fig. 3 and the Appendix for their definitions and resulting harmonic components).

One can further improve the dynamic stall modeling by introducing "stall delay time"[16,18] in the nonlinear lift part of the ONERA equations. This is equivalent to assuming that no stall will occur during the delay time $\Delta\tau$ after the angle of attack has passed the stall angle α_Δ. The stall delay can be implemented in the current harmonic model by simply taking out an initial part of the stalled region in the Fourier integrals. A delay of $\Delta\tau = 10$ in the nondimensional time seems accepted,[18] and so this value is used in the present analysis.

After completing the Fourier analysis of the deviations ΔC_z, these harmonic expressions are substituted into Eqs. (11-14) to yield the harmonic components of the circulations, Γ_{1z}, Γ_{2z}, and Γ_{D1}, Γ_{D2}. These components then define the circulatory lift, moment, and drag.[10] It is mentioned that in calculating the coefficients a_z, r_z, e_z, and a_D, r_D, e_D for the nonlinear part of the ONERA equations, the lift deviation ΔC_L has been replaced by its time averaged part ΔC_{L0} to avoid computational complexity. Naturally, one should expect that as the angle of attack and the reduced frequency become higher, this approximation will degrade the Fourier analysis.

VI. Method of Solution

In this section, a solution technique for nonlinear large amplitude flutter that evolves from linear flutter solutions is described. To obtain a complete solution of the nonlinear problem, one first finds the linear flutter points. This preliminary procedure involves finding a static position of the rotor blade given a rotational speed Ω and a root pitch angle θ_r, then checking the aeroelastic stability of the blade about the solved static position. The static solution is obtained by dropping dynamic terms and integrating the resulting 12 differential equations with appropriate tip boundary values. The linear flutter solution can be found by retaining only the first-order

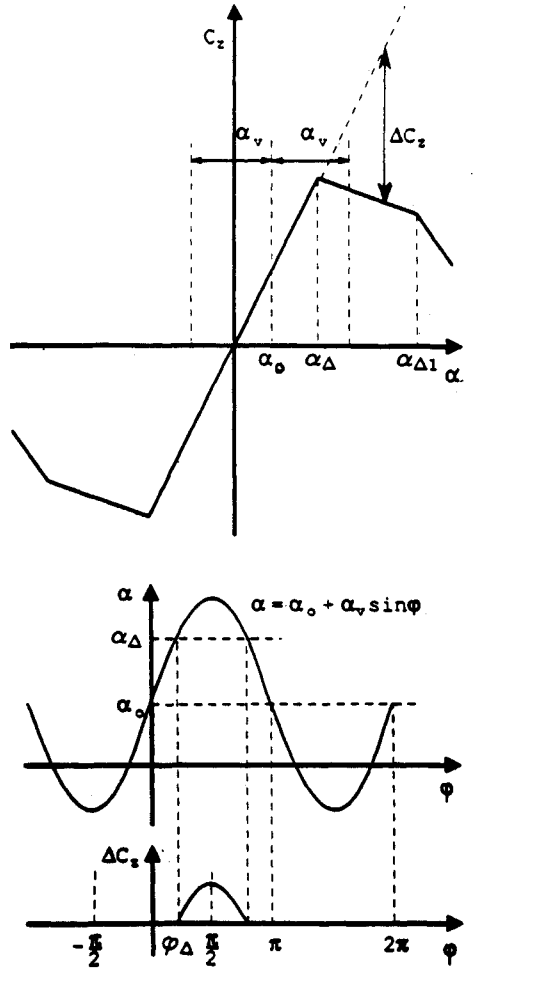

Fig. 3 Example of oscillation stall angle on aerodynamic curve and in phase domain.

dynamic terms around the solved static position and applying a transfer matrix method to the resulting 24 linear equations.[10]

Unlike its linear counterpart, the nonlinear flutter problem is coupled with static parts of the solution. Furthermore, there is one-to-one correspondence between a pair of given (Ω, ω) and an amplitude level of the solution. Thus, one can express the coupled nonlinear differential equations in vector form

$$\frac{dX_0}{ds} = h_0(X_0, X_s, X_c, \Omega, \omega) \qquad (29)$$

$$(12 \times 1) \qquad (12 \times 1)$$

and

$$\frac{dX_s}{ds} = h_s(X_0, X_s, X_c, \Omega, \omega) \qquad (30)$$

$$(12 \times 1) \qquad (12 \times 1)$$

$$\frac{dX_c}{ds} = h_c(X_0, X_s, X_c, \Omega, \omega) \qquad (31)$$

$$(12 \times 1) \qquad (12 \times 1)$$

where

$$X_0 = [F_{10}\ F_{20}\ F_{30}\ M_{10}\ M_{20}\ M_{30}\ x_0\ y_0\ z_0\ \theta_0\ \beta_0\ \psi_0]^T$$

$$X_s = [F_{1s}\ F_{2s}\ F_{3s}\ M_{1s}\ M_{2s}\ M_{3s}\ x_s\ y_s\ z_s\ \theta_s\ \beta_s\ \psi_s]^T$$

$$X_c = [F_{1c}\ F_{2c}\ F_{3c}\ M_{1c}\ M_{2c}\ M_{3c}\ x_c\ y_c\ z_c\ \theta_c\ \beta_c\ \psi_c]^T$$

The vector function arrays h_0, h_s, and h_c contain many product terms involving multiplications of two or three harmonic quantities. They originate from the 12 basic equations that are presented in Refs. 8 and 9. Multiplications of harmonics and calculations of the coefficients of the resulting new harmonics can be implemented according to formulas similar to the ones in the Appendices of Ref. 9.

To solve this system, all of the 36 equations (now 12 for the static part, 24 for the dynamic part) are first integrated once from the tip to the root of the blade. To start the numerical integration, one has to guess the tip boundary value X_t as well as the rotational speed Ω and frequency ω that will make X_r at the root as close to the prescribed values as possible. Since the nonlinear solutions are assumed to evolve from linear solutions, the eigensolution and Ω, ω obtained earlier in the linear aeroelastic analysis are used for the initial X_t. The functional relationships between these two sets of boundary values can be written as

$$X_r = f(X_t, \Omega, \omega) \qquad (32)$$

$$(18 \times 1) \qquad (18 \times 1)$$

where

$$X_t = [x_0\ x_s\ x_c\ y_0\ y_s\ y_c\ z_0\ z_s\ z_c\ \theta_0\ \theta_s\ \theta_c\ \beta_0\ \beta_s\ \beta_c\ \psi_0\ \psi_s\ \psi_c]^T$$

$$X_r = [0\ 0 \ldots 0\ \theta_r\ 0 \ldots 0]^T$$

at the tip and root, respectively. Since for a given level of amplitude, the initial 18 components of X_t are not exact, a Newton-Raphson algorithm is employed to produce a better set of boundary values based on the current values, namely,

$$X_t^{n+1} = X_t^n - J(X_t^n, \Omega^n, \omega^n)^{-1} R^n \qquad (33)$$

where

$$R^n \equiv f(X_t^n, \Omega^n, \omega^n) - X_r$$

J: (18×18) Jacobian matrix

This algorithm must take iterations on the Ω and ω as well as the boundary values, since it is not known in advance at which rotational speed and frequency a nonlinear flutter will exist for a given amplitude level. Therefore, one of the sine parts of the boundary amplitudes at the tip x_s, y_s, z_s, θ_s is replaced by Ω and is fixed at a given value throughout the iterations. Also, the corresponding cosine part of that boundary amplitude is replaced by ω and is fixed at zero, since the associated phase of the flutter can be assigned any value. Which pair of amplitude should be replaced depends on the flutter mode shape of interest; but the torsional amplitude pair (θ_s, θ_c) is usually chosen.

For each amplitude level, the iteration stops when the residue vector R at the root becomes sufficiently small. Beginning with a very small amplitude level which essentially corresponds to the linear flutter solution, the solution method marches with increased amplitude until where the algorithm diverges, i.e., there exists no solution.

VII. Results and Discussion

The prescribed structural and aerodynamic modeling and solution technique have been applied to a two-bladed model of $[0/90]_{3S}$ graphite/epoxy layup with zero preconing angle and zero hinge offset. This blade, 560 mm in span and 30 mm in chord, has been used previously by Minguet and Dugundji[8] and Kim and Dugundji[9] for both analysis and experiment. Its stiffness properties are listed in Ref. 10. The blade exhibits rotating lag frequencies ranging from 4 to 6 per revolution and rotating torsional frequencies from 7 to 10 per revolution over the rotational speeds investigated, hence can be categorized as a hard in-plane blade. Warping and transverse shear were not included in the results since they were expected to be small here. A total of eight equally distributed node points were used along the blade. Occasionally, convergence was checked by using 16 node points instead. All of the runs were made on an IBM RSAIX 6000 computer with typical number of iterations from 10 to 20 for convergence.

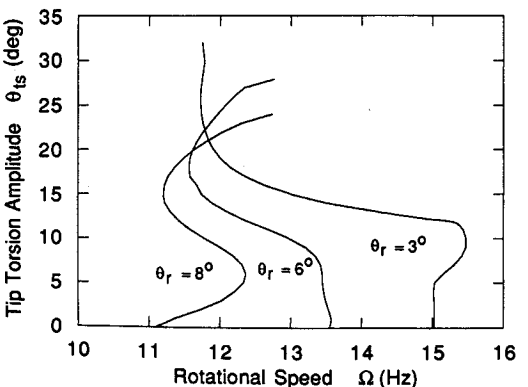

Fig. 4 $[0/90]_{3S}$ tip torsion amplitude vs rotational speed.

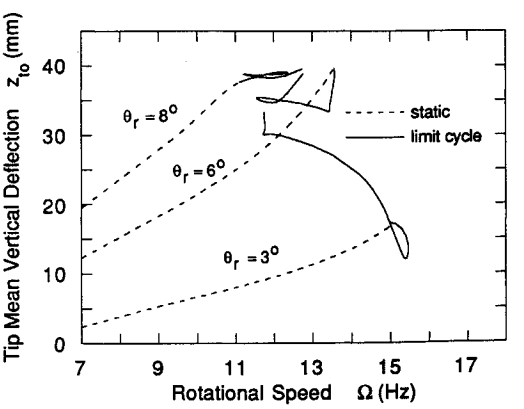

Fig. 5 $[0/90]_{3S}$ tip mean vertical deflection vs rotational speed.

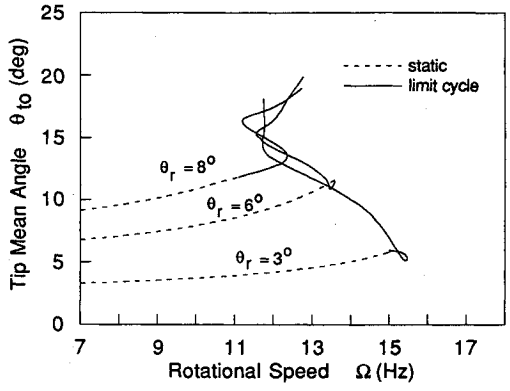

Fig. 6 $[0/90]_{3S}$ tip mean angle vs rotational speed.

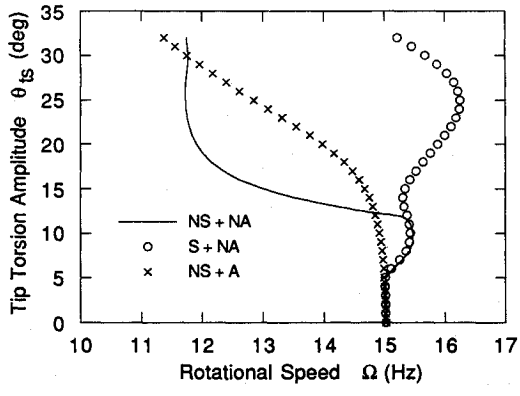

Fig. 7 $[0/90]_{3S}$ tip torsion amplitude vs rotational speed, $\theta_r = 3$ deg.

Figures 4–6 show the following information on flutter corresponding to three root pitch angles, 3, 6, and 8 deg within each plot: a) the variation of tip torsional vibration amplitude θ_{ts} with rotational speed Ω, b) the variation of tip mean vertical deflection z_{t0} with Ω, and c) the variation of tip mean angle θ_{t0} with Ω. Also shown in b) and c) in dashed lines are static curves when no flutter limit cycles are present. Thus, all of the limit cycle results start at linear flutter points where dashed and solid curves coincide, and the analysis continues with increasing torsional vibration amplitude level. The flutter frequencies were about 3 per revolution for these cases.

The first case with 3 deg of root pitch is initially in the unstalled region (mean angle of attack at the tip α_{t0} is 3.5 deg) beginning at a rotational speed of 15.0 Hz at the onset of flutter, and then entering into the stall region at approximately 5 deg of the tip torsional amplitude. This is indicated by the sharp turn at $\theta_{ts} = 5$ deg after a straight vertical branch in the amplitude vs Ω plot (Fig. 4), and initial sharp decreases in the corresponding tip mean vertical deflection (Fig. 5), and tip mean angle (Fig. 6).

The sharp turn at the beginning of dynamic stall could be termed as "hardening," i.e., increase in rotational speed will result in increase in the amplitude. The sudden drop in the mean deformations at the start of this hardening is caused by loss of static lift and moment associated with the initiation of dynamic stall. After the stall occurs, however, beginning at about $\theta_{ts} = 10$ deg, the mean deformations seem to increase continuously. The cases with 6 and 8 deg of root pitch are initially in the stalled region ($\alpha_{t0} = 8.1$ and 8.4 deg, respectively), i.e., an outer portion of the blade has been stalled statically before flutter begins. Here, the flutter starts at rotational speeds lower than the unstalled case due to destabilizing effects of the unsteady aerodynamic coefficients for small amplitude motion about a stalled angle of attack. Still, the second case with 6 deg of root pitch shows a similar trend as the first case in the mean deformations. Both softening and hardening trends could occur in the amplitude vs critical speed characteristics depending on root pitch and amplitude level. In particular, there is strong hardening at low root pitch (3 deg) and high root pitch (8 deg) in the amplitude region after the blade stalls. At moderate to large amplitude levels, a softening trend occurs in all three cases, but at still higher amplitude levels, a hardening is seen to reappear. However, in view of the previous discussion regarding aerodynamic hysteresis generated by the ONERA model, all the results at the higher amplitude levels should be regarded with caution.

Figures 7–9 show the relative effects of the structural nonlinearities and the aerodynamic nonlinearities (dynamic stall) on the flutter characteristics of the blade. For comparison purpose these figures show, for the 3 deg of root pitch, a) the full analysis with the nonlinear structure and the nonlinear aerodynamics (NS + NA), b) an analysis combining linearized structure and the nonlinear aerodynamics (S + NA), and c) an analysis combining the nonlinear structure and the linear aerodynamics excluding the stall effects (NS + A). From the figures, it appears that the initial hardening phenomenon mentioned earlier is mainly attributed to the aerodynamic part; here, the linearized structure with dynamic stall seems accurate enough to capture the hardening effect whereas the linear aerodynamics completely misses it. This initial hardening is due to increases in "effective" aerodynamic damping coefficients in both the plunging and pitching motions, associated with the lift and moment hysteresis loops at high amplitude levels. In other words, the large amplitude motion that crosses between the unstalled and stalled regions generally yields an increase in the overall aerodynamic damping, and, thereby results in stabilizing (hardening) effects. As the amplitude level is increased further, however, there appears strong softening in all of the branches, and the dynamic stall does not seem to capture the trend; curiously, the nonlinear structure with linear aerodynamic theory is able to predict this to a certain extent, suggesting that the softening mostly stems from the structure, not from the aerodynamics. To provide a ratio-

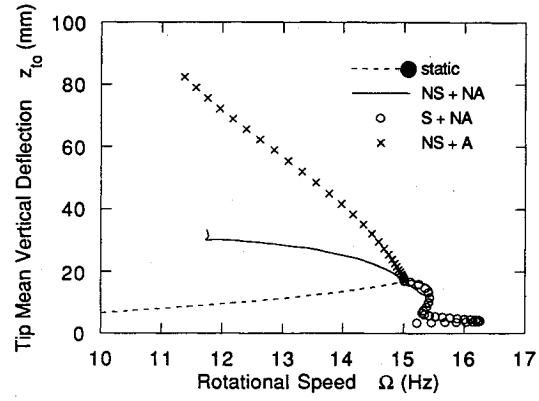

Fig. 8 $[0/90]_{3S}$ tip mean vertical deflection vs rotational speed, $\theta_r = 3$ deg.

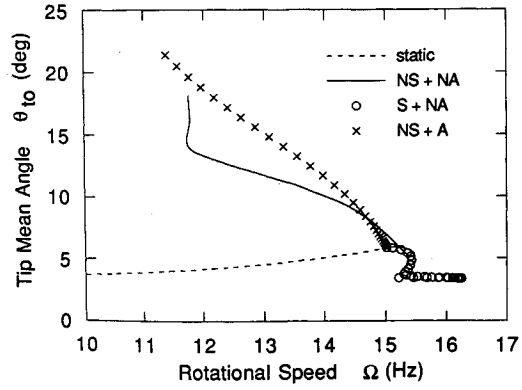

Fig. 9 $[0/90]_{3S}$ tip mean angle vs rotational speed, $\theta_r = 3$ deg.

nale for such an adverse phenomenon, it is recalled that there is a strong coupling between the torsion and lag motions when the blade bends vertically. As shown in Kim and Dugundji,[9] for increasing vibration levels in the presence of a moderate amount of static tip deflection, the lag mode can undergo a significant increase in its mean position z_{t0} at the tip and a decrease in its frequency. The flutter frequencies in these calculations suggest those of the first fore-and-aft (lag) mode. Thus, this structural softening of the lag mode could largely be the source of the dramatic aeroelastic softening in the high range of amplitudes found in Fig. 4. The structural softening effect becomes more dominant and seems to pervade into the low amplitude region at high root-pitch angle or when the blade is initially stalled.[10]

From the structural point of view, it is not surprising that the nonlinear structure with linear aerodynamics in the entire amplitude region yields softening results accompanied by center shift rises, due to the flutter mode being close to the first fore-and-aft mode shape of free vibration. On the other hand, the linearized structure with dynamic stall analysis seems to yield merely hardening results in most of amplitude range, and hardly regains z_{t0} once the stall starts as a result of lift and moment loss associated with the dynamic stall.

VIII. Conclusion

Investigation of the nonlinear large amplitude aeroelastic behavior of hingeless composite rotor blades, in the simple case of hover, has been performed using 12 differential equations based on the use of Euler angles together with a harmonic balance, finite difference, and Newton-Raphson iteration technique. The large amplitude effect in the structure was included by expanding the transformation matrix elements about large static angles and the rotations up to third order in terms of dynamic counterparts. The large amplitude effect in the aerodynamics, i.e., the dynamic stall, was included by the ONERA model and low Reynolds number stall characteristics of a NACA 0012 airfoil.

The linear flutter solutions were first obtained by the transfer matrix method, and large amplitude solutions that evolve from these linear solutions were sought. The method, when applied to a two-bladed example of $[0/90]_{3S}$ layup, gave results that show the dominant effect of the dynamic stall in the moderate range of amplitudes, but the equally strong effect of the nonlinear structure in the higher range of amplitudes. The effect of the nonlinear aerodynamics is found almost always hardening in bringing up the dynamic pressure levels required to sustain given amounts of amplitudes. On the contrary, when the large amplitude flutter modes exhibit strong couplings between lead-lag and torsional motion, the static-dynamic couplings in the structure give rise to a strong softening effect.

The present paper has developed a methodology for dealing with nonlinear, large amplitude aeroelastic problems of rotor blades. The initial blade model chosen in this paper exhibits lag mode frequencies which are higher than typical hard in-plane rotor blades. Therefore, all of the aeroelastic results found in the paper are likely related to hingeless hard in-plane rotating blades and should only represent qualitatively the nonlinear characteristics of such blades. Since soft in-plane rotor blades may have different types of flutter modes with a lesser degree of lag-torsion coupling, different nonlinear trends may be expected of these blades. Additional research needs to be performed on various types of blades, with more realistic blade specifications and more reliable dynamic stall characteristics.

Appendix: Fourier Analysis of ΔC_z and ΔC_D

Fourier analysis of lift, moment, and drag deviations are given. First, the definitions are given for ΔC_z.

$$\Delta C_L = 0 \quad \text{if} \quad \alpha \le \alpha_\Delta$$

$$\Delta C_L = 6.32284(\alpha - \alpha_\Delta) \quad \text{if} \quad \alpha_\Delta < \alpha \le \alpha_{\Delta 1}$$

$$\Delta C_L = 6.32284(\alpha - \alpha_\Delta) - 0.42284(\alpha - \alpha_{\Delta 1}) \quad \text{if} \quad \alpha > \alpha_{\Delta 1}$$

$$\Delta C_M = 0 \quad \text{if} \quad \alpha \le \alpha_\Delta$$

$$\Delta C_M = 0.65317(\alpha - \alpha_\Delta) \quad \text{if} \quad \alpha_\Delta < \alpha \le \alpha_{\Delta 1}$$

$$\Delta C_M = 0.65317(\alpha - \alpha_\Delta) - 0.48128(\alpha - \alpha_{\Delta 1}) \quad \text{if} \quad \alpha > \alpha_{\Delta 1}$$

where $\alpha_\Delta = 8$ deg and $\alpha_{\Delta 1} = 18$ deg.

For ΔC_D, the following cubic form was assumed:

$$\Delta C_D = -0.042\alpha - 0.1473\alpha^2 - 4.923\alpha^3$$

For simplicity, a single-breakpoint model with positive stall part is illustrated for the harmonic analysis of the lift and moment deviations.

For a single-breakpoint model of lift and moment deficiencies

$$\Delta C_z = a_{11z}(\alpha - \alpha_\Delta) \quad \text{for} \quad \alpha \ge \alpha_\Delta$$

$$\Delta C_z = 0 \quad \text{for} \quad \alpha \le \alpha_\Delta$$

the Fourier integrals (28) give

$$\Delta C_{z0} = (a_{11z}/\pi)[(\alpha_0 - \alpha_\Delta)\{\pi/2 - \tfrac{1}{2}(\varphi_\Delta + \varphi_{\Delta 1})\} + (\alpha_V/2)(\cos\varphi_\Delta + \cos\varphi_{\Delta 1})]$$

$$\Delta C_{zVs} = -(a_{11z}\alpha_V/\pi)[\tfrac{1}{2}\sin\varphi_\Delta\cos\varphi_\Delta + \cos\varphi_{\Delta 1} \times (\sin\varphi_\Delta - \tfrac{1}{2}\sin\varphi_{\Delta 1}) - (\pi/2) + \tfrac{1}{2}(\varphi_{\Delta 1} + \varphi_\Delta)]$$

$$\Delta C_{zVc} = (a_{11z}\alpha_V/\pi)[\sin\varphi_\Delta(\sin\varphi_{\Delta 1} - \sin\varphi_\Delta) + \tfrac{1}{4}(\cos 2\varphi_{\Delta 1} - \cos 2\varphi_\Delta)]$$

where

$$\varphi_\Delta = \frac{\pi}{2}\,(\text{no stall}) \quad \text{if} \quad \frac{\alpha_\Delta - \alpha_0}{\alpha_V} > 1$$

$$= -\frac{\pi}{2}\,(\text{full stall}) \quad \text{if} \quad \frac{\alpha_\Delta - \alpha_0}{\alpha_V} < -1$$

$$= \sin^{-1}\left(\frac{\alpha_\Delta - \alpha_0}{\alpha_V}\right)\left(\text{partial stall}\right) \text{ elsewhere}$$

$$\varphi_{\Delta 1} = \varphi_\Delta\,(\text{no stall}) \quad \text{if} \quad \frac{\alpha_\Delta - \alpha_0}{\alpha_V} > 1$$

$$= \varphi_\Delta\,(\text{full stall}) \quad \text{if} \quad \frac{\alpha_\Delta - \alpha_0}{\alpha_V} < -1$$

$$= \varphi_\Delta + 10k\ (\text{partial stall}) \text{ elsewhere}$$

Also, φ_Δ and $\varphi_{\Delta 1}$ are set to $(\pi/2)$ if $\varphi_{\Delta 1} > \pi - \varphi_\Delta$; in this case the stall delay time is long enough not to initiate the stall.

To further account for negative stall, a symmetric aerodynamic force curve can be employed by including a second stall angle at $-\alpha_\Delta$. The resulted formula is not shown here.

For the drag stall part, the Fourier integrals reduce to

$$\Delta C_{D0} = (2/\pi)[-0.042(-\alpha_0\varphi_1 + \alpha_V\cos\varphi_1) - (\pi/2)0.1473 \times (\alpha_0^2 + \tfrac{1}{2}\alpha_V^2) - 4.923\{-\alpha_0^3\varphi_1 + 3\alpha_0^2\alpha_V\cos\varphi_1 + (3/2)\alpha_0\alpha_V^2 \times (-\varphi_1 + \sin\varphi_1\cos\varphi_1) + (\alpha_V^3/3)\cos\varphi_1(\sin^2\varphi_1 + 2)\}]$$

$$\Delta C_{DVs} = (4/\pi)\big[-0.042\{\alpha_0\cos\varphi_1 + (\alpha_V/2) \times (-\varphi_1 + \sin\varphi_1\cos\varphi_1)\} - (\pi/2)0.1473\alpha_0\alpha_V - 4.923\{\alpha_0^2\cos\varphi_1 + (3/2)\alpha_0^2\alpha_V(-\varphi_1 + \sin\varphi_1\cos\varphi_1) + \alpha_0\alpha_V^2\cos\varphi_1(\sin^2\varphi_1 + 2) + \alpha_V^3[-(3/8)\varphi_1 + \tfrac{1}{2}\sin\varphi_1\cos\varphi_1 - \tfrac{1}{8}\sin\varphi_1\cos\varphi_1\cos 2\varphi_1]\}\big]$$

$$\Delta C_{DVc} = 0$$

where

$$1 = -(\pi/2) \quad \text{if} \quad \alpha_V < |\alpha_0|$$

$$= -\sin^{-1}(\alpha_0/\alpha_V) \quad \text{if} \quad \alpha_V > |\alpha_0|$$

References

[1]Chopra, I., and Dugundji, J., "Non-linear Dynamic Response of a Wind Turbine Blade," *Journal of Sound and Vibration,* Vol. 63, No. 2, 1979, pp. 265–286.

[2]Dunn, P. E., and Dugundji, J., "Nonlinear Stall Flutter and Divergence Analysis of Cantilevered Graphite/Epoxy Wings," *AIAA Journal,* Vol. 30, No. 1, 1992, pp. 153–162.

[3]Tran, C. T., and Petot, D., "Semi-Empirical Model for the Dynamic Stall of Airfoils in View of their Application to the Calculation of Responses of a Helicopter Rotor in Forward Flight," *Vertica,* Vol. 5, No. 1, 1981, pp. 35–53.

[4]Tang, D., and Dowell, E., "Experimental and Theoretical Study for Nonlinear Aeroelastic Behavior of Flexible Rotor Blades," AIAA Paper 92-2253, April 1992.

[5]Hodges, D. H., and Dowell, E. H., "Nonlinear Equations of Motion for the Elastic Bending and Torsion of Twisted Non-uniform Rotor Blades," NASA TN D-7818, Dec. 1974.

[6]Loewy, R. G., Rosen, A., and Mathew, M. B., "Application of the Principal Curvature Transformation to Nonlinear Rotor Blade Analysis," *Vertica,* Vol. 11, No. 1/2, 1987, pp. 263–296.

[7]Mathew, M. B., and Loewy, R. G., "Nonlinear Effects in Helicopter Rotor Forward Flight Forced Response," *Vertica,* Vol. 14, No. 1, 1990, pp. 1–18.

[8]Minguet, P. J., and Dugundji, J., "Experiments and Analysis for Composite Blades Under Large Deflections. Part 1: Static Behavior, Part 2: Dynamic Behavior," *AIAA Journal,* Vol. 28, No. 9, 1990, pp. 1573–1588.

[9]Kim, T., and Dugundji, J., "Nonlinear Large Amplitude Vibrations of Composite Helicopter Blade at Large Static Deflection," *AIAA Journal,* Vol. 31, No. 5, 1993, pp. 938–946.

[10]Kim, T., "Nonlinear Large Amplitude Structural and Aeroelastic Behavior of Composite Rotor Blades at Large Static Deflection," Ph.D. Thesis, Dept. of Aeronautics and Astronautics, Massachusetts Inst. of Technology, Cambridge, MA, May 1992.

[11]Friedmann, P. P., "Helicopter Rotor Dynamics and Aeroelasticity: Some Key Ideas and Insights," *Vertica,* Vol. 14, No. 1, 1990, pp. 101–121.

[12]Crawley, E. F., and Dugundji, J., "Frequency Determination and Non-Dimensionalization for Composite Cantilever Plates," *Journal of Sound and Vibration,* Vol. 72, No. 1, 1980, pp. 1–10.

[13]Tran, C. T., and Falchero, D., "Application of the ONERA Dynamic Stall Model to a Helicopter Blade in Forward Flight," *Vertica,* Vol. 6, No. 3, 1982, pp. 219–239.

[14]Rogers, J. P., "Application of an Analytic Stall Model to Time History and Eigenvalue Analysis of Rotor Blades," *Journal of the American Helicopter Society,* Vol. 29, No. 1, 1984, pp. 25–33.

[15]Peters, D. A., "Toward a Unified Lift Model for Use in Rotor Blade Stability Analysis," *Journal of the American Helicopter Society,* Vol. 30, No. 3, 1985, pp. 32–42.

[16]Petot, D., and Dat, R., "Unsteady Aerodynamic Loads on an Oscillating Airfoil with Unsteady Stall," 2nd Workshop on Dynamics and Aeroelasticity Stability Modeling of Rotorcraft Systems, Florida Atlantic Univ., Boca Raton, FL, Nov. 1987.

[17]Barwey, D., Gaonkar, G. H., and Ormiston, R. A., "Investigation of Dynamic Stall Effects on Isolated Rotor Flap-Lag Stability with Experimental Correction," *Journal of the American Helicopter Society,* Vol. 36, No. 4, 1991, pp. 12–24.

[18]McAllister, K. W., Pucci, S. L., McCroskey, W. J., and Carr, L.W., "An Experimental Study of Dynamic Stall on Advanced Airfoil Section," NASA TM 84245, Sept. 1982.